RESEARCH ARTICLE | JULY 11 2023

Skipping under water: Buoyant sphere hydrodynamics at the air–water interface ⓕ

Farrukh Kamoliddinov ; Ivan U. Vakarelski ; Sigurdur T. Thoroddsen ; Tadd T. Truscott ✉

Check for updates

View Online

Export Citation

Physics of Fluids

Special Topic:
Recent Advances in Fluid Dynamics and its Applications

Guest Editors: B.Reddappa, B. Rushi Kumar, Sreedhara Rao Gunakala, Bijula Prabhakar Reddy

Submit Today!

AIP Publishing

AIP Publishing

Skipping under water: Buoyant sphere hydrodynamics at the air–water interface ⓕ

View Online　　Export Citation　　CrossMark

Farrukh Kamoliddinov,[1] ⓘ Ivan U. Vakarelski,[2] ⓘ Sigurdur T. Thoroddsen,[1] ⓘ and Tadd T. Truscott[1,a] ⓘ

AFFILIATIONS

[1]Division of Physical Sciences and Engineering, Mechanical Engineering, King Abdullah University of Science and Technology (KAUST), Thuwal 23955-6900, Saudi Arabia
[2]Department of Chemical and Pharmaceutical Engineering, Faculty of Chemistry and Pharmacy, Sofia University, 1 James Bourchier Avenue, 1164 Sofia, Bulgaria

[a]Author to whom correspondence should be addressed: taddtruscott@gmail.com

ABSTRACT

We present an experimental study of the hydrodynamics of a buoyant sphere accelerated horizontally along an air–water interface. At low speeds, the sphere floats at the surface, while at higher speeds, the sphere starts oscillating, moving below and toward the free surface akin to underwater skipping. The sphere often breaches and forms an air cavity during its subsequent dive. These underwater air cavities become horizontal and are attached to the sphere surface near the laminar flow separation point ($\sim \pi/2$). High-speed imaging is used to investigate the effects of changing the pulling angle and counterweight-induced velocity on the hydrodynamics. We examine the transition from underwater skipping oscillations to water exit, particularly above the critical Froude number of 1.2, where buoyant spheres experience complex fluid–solid interactions revealing the influence of the air cavity on drag and lift coefficients and overall sphere hydrodynamics. Finally, we analyze the novel phenomenon of the steady motion of the horizontally pulled sphere with an attached inverted-wing-shaped air cavity.

I. INTRODUCTION

The dynamics of structures impacting water surfaces have been extensively studied by researchers due to their wide range of engineering applications. Skipping stones,[1] bouncing balls,[2] and the ability to walk on water, as exhibited by basilisk lizards[3] and some birds,[4] are fascinating natural phenomena that have captivated the attention of many scientists. When objects impact the water surface with sufficient velocity, appropriate geometry, and orientation, they carve an air cavity into the air–water interface due to the effects of hydrodynamic pressure.[5] Skipping at the air–water interface occurs when the object generates a large enough upward vertical force to lift off.[6] The physics of stone skipping was studied by Bocquet[7] and Rosellini *et al.*,[8] who showed that the maximum number of skips is a function of the stone's speed, angular velocity (stability), attack angle, and angle of the impact velocity. Belden *et al.*[2] studied the bouncing and skipping mechanisms of elastic spheres on water surfaces using experimental and numerical simulations. They found that the dynamics of elastic sphere bouncing and skipping are driven by the ratio of material shear modulus to hydrodynamic pressure and wave propagation speed. Hurd *et al.*[9] experimentally demonstrated a new mode of skipping, water walking

on the water surface, for relatively soft spheres impacting at low angles and found a good agreement between the measured acceleration, number of skipping events, and distance traveled.

In our previous work,[10] we investigated the hydrodynamics of a buoyant sphere pulled horizontally along an air–water interface. We attached the sphere to a line and pulley system, which enabled us to vary the pulling force by changing a falling mass. This setup was nearly identical to the one shown in Fig. 1. We identified three hydrodynamic regimes based on the Froude number, $Fr = U/\sqrt{gR}$, where U is the sphere velocity, g is the gravity, and d is the sphere diameter. At the low Froude number regime ($Fr < 0.6$), the sphere exhibits little water surface disturbance and experiences a drag force close to half of a fully submerged sphere. In the intermediate regime ($0.6 < Fr < 1.2$), a distinct wave pattern develops, and the sphere dips below the water level, increasing the drag force. At the highest regime ($Fr > 1.2$), the sphere transitions to a mode of periodic dipping below and surfacing above the water surface.

In the current study, we use the same setup as our previous study to investigate the hydrodynamics of a floating sphere pulled with even larger pulling forces (e.g., Froude numbers from 2 to 15) and add
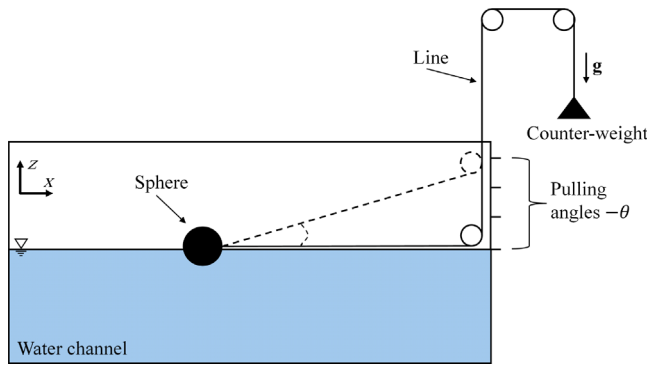
FIG. 1. A schematic of the experimental setup consisting of a water channel, four pulling angles, and a counterweight that pulls the buoyant sphere along the air–water interface.

multiple pulling angles relative to the air–water interface (see Fig. 1). These spheres appear to approach the surface and skip below or pass through the free surface into the air. We find that the spheres can form a horizontal air cavity as they transition from underwater skipping (oscillations) to water exit as $Fr > 1.2$, where higher pulling angles result in longer air cavities, larger skipping distances, and earlier water exit behavior.

The current work extends the understanding of the behavior of objects along the air–water interface and sheds light on the complex hydrodynamics involved in the formation of horizontal air cavities and the transition from the floating to the skipping mode. This knowledge has implications for numerous real-world applications, such as developing underwater vehicles, ship design, buoys, and other oceanographic instruments that are used to study and/or rescue marine animals and their behavior.

II. EXPERIMENTAL OVERVIEW

A schematic of the experimental setup is shown in Fig. 1. Experiments were carried out in the KAUST water channel, which is 10 m long and has a 1×1 m cross section (see supplementary material, Fig. S1). The channel's walls and bottom are made from transparent clear acrylic, and the channel is 1 m above the lab floor, allowing simultaneous bottom- and side-view observations. In most experiments, the channel was half full of water with a depth of about 50 cm, which eliminates splashing outside the tank due to the impact of the spheres at high velocities.

We use a hollow aluminum sphere of $d = 5$ cm diameter, with a density ratio of $\rho^* = \rho_s / \rho_w = 0.75$, where ρ_s is the density of the sphere and ρ_w is the density of water. The sphere surface was drilled with a small hole symmetrically positioned to attach a nylon fishing line (diameter $\sim$3 mm) in order to drag it through the water surface (Fig. 1). The line is fixed to a pulley system with adjustable pulling angles and counterweights, varying the pulling force by adjusting their mass. Before each set of measurements, the sphere was thoroughly cleaned with ethanol, and the same sphere was used throughout all experiments. Pulling counterweight forces varied from $F_{cw} = 7$ to 12 N with four pulling angles, $\theta = 0°$–5.15° from the sphere's release point, which is $\sim$5 m from the roller at the end of the channel. The spheres were released from floating on the free surface, and its movement was tracked for $\sim$3 m in all experiments using side-view imaging with
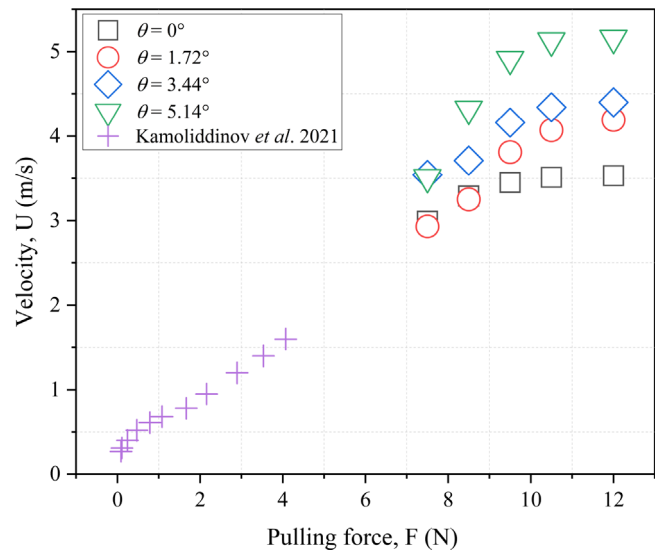

FIG. 2. Relationship between the average velocity U and the pulling counterweight forces F_{cw} from our previous study[10] ($\theta = 0$), combined with the results of the current study for all pulling angles θ. The velocity increases for all pulling angles as the pulling counterweight force increases.

backlighting. The surface of the clean and dried sphere is hydrophilic and exhibits a static water contact angle of approximately 35°. We do not expect hydrophobicity to make the sphere any easier to jump out of the water as was shown by Truscott et al.;[11] however, one may expect more consistent re-entry cavity sizes if the surfaces were hydrophobic, which was not studied here.

Figure 2 summarizes the relationship between the average velocity U and the pulling counterweight forces F_{cw} for all the pulling angles used in our study. The resulting sphere velocity magnitudes range from $\bar{u} = 1$ to 8 m/s. Table I summarizes the dimensions and parameters of this study. The specific gravity of the sphere used in our previous study was 0.5 compared to 0.75 here, as the diameter is now half the size. A smaller sphere was used in this study because of the limitations of the tank length and pulling force requirements for speed increases. The pulling forces produced by the counterweights were determined using an extrapolation based on calibration using Hooke's law outlined in our previous study.[10] The pulling force $F = mg - F_{fr}$, where m is the counterweight mass and F_{fr} is the combined pulley and friction forces. Since F_{fr} is not known in our system, we employed a set

TABLE I. Summary of dimensional and non-dimensional parameters relevant to this study.

Parameters	Symbol	Range/values	Units
Sphere diameter	d	5	cm
Pulling angle	θ	0, 1.72, 3.44, 5.14	(°)
Counterweight	F_{cw}	7, 8.5, 9.5, 10.5, 12	N
Reynolds number	Re	$1.2 - 2.6 \times 10^5$	–
Froude number	Fr	$2 - 15$	–
Velocity magnitude	$\bar{u}$	$1 - 8$	m/s

of calibrated springs to calculate the pulling force for each counter-weight mass used in the study.

High-speed video imaging was used to determine the instantaneous velocity of the sphere in the x and z directions. To capture longer sections of the sphere's trajectory, we used two simultaneous high-speed cameras from two adjacent side views: Photron-FASTCAM-SA5 and FASTCAM-SA3, with 20 and 55 mm lenses with a resolution of 1024×1024 pixels (i.e., resolution of 3.0, and 1.0 mm/pixel, respectively). The cameras were positioned to capture the sphere's motion at the air–water interface from the release point to the end of the tank. The videos were taken with a typical rate of $250 - 2000$ frames per second (fps) with a shutter speed of up to 1/8000 s to reduce motion blur.

We use the regular definition of the drag coefficient, $C_D = 2F_D/\pi R^2 \rho U^2$, as for a fully submerged sphere, even though, in our case, the sphere was not always completely submerged in water. Here, R is the sphere radius, U is the sphere velocity, and ρ is the water density. The Froude and Reynolds numbers are defined: $Fr = U/\sqrt{gd}$ and $Re = \rho d U/\mu$, where g is the gravity, d is the sphere diameter, and μ is the dynamic viscosity.

III. RESULTS AND DISCUSSION

A. Pulling angles and cavity formation

Two of the experimental cases, $F_{cw} = 7$ and 9.5 N, were selected to analyze the hydrodynamic mechanisms of an accelerated sphere pulled along an air–water interface with different pulling angles. There is no particular reason for choosing these cases except to show how increasing force alters the behavior (see supplementary material for more cases). Figures 3(a) and 3(b) (Multimedia view) show the sphere trajectories of these two cases extracted from experimental videos in the x–z planes, using side-view video observations. The x and z positions are normalized by the sphere diameter d, and the free surface corresponds to a value of $z/d = 0$. We observe three different hydrodynamic behaviors: (1) oscillatory movement of the sphere below and up to the water surface (e.g., $x/d = 0$–40 for $\theta = 0°$), (2) generation and pull-down of a horizontal air cavity (e.g., $x/d = 10$–15 for $\theta = 3.44°$), and (3) the sphere exits out of the water surface (e.g., $x/d = 42$ for $\theta = 3.44°$). Figure 4 (Multimedia view) shows a time series of images illustrating each of these hydrodynamic behaviors. Comparison plots of multiple runs are shown in Figs. S6 and S7 to highlight the reproducibility of the experiment. In contrast to our first paper, these spheres experience larger velocities (Fig. 2). Consequently, the vortex shedding is no longer the same in all directions and in time. This results in larger variations in the results, where in one run, the vortex may be shed from the far side of the sphere, and in another, it may shed from the bottom at a slightly different time. In our first paper, the velocities were much slower and the sphere meandered on the surface for most of the cases, where vortex shedding was influenced by the free surface and more consistently shed from a specific location.

The side-view trajectories for $\theta = 0°$ in Figs. 3(a) and 4(I) show that the movement in the x–z-planes oscillates the most below the surface (two times), while for the larger pulling, weight in (b) at $\theta = 0°$ also oscillates but with smaller amplitudes never reaching the water surface until the end of the run, where the sphere is near the pulley. The multiple underwater oscillations are repeatable only for the $\theta = 0°$ cases. The oscillation pattern is also observable in velocity
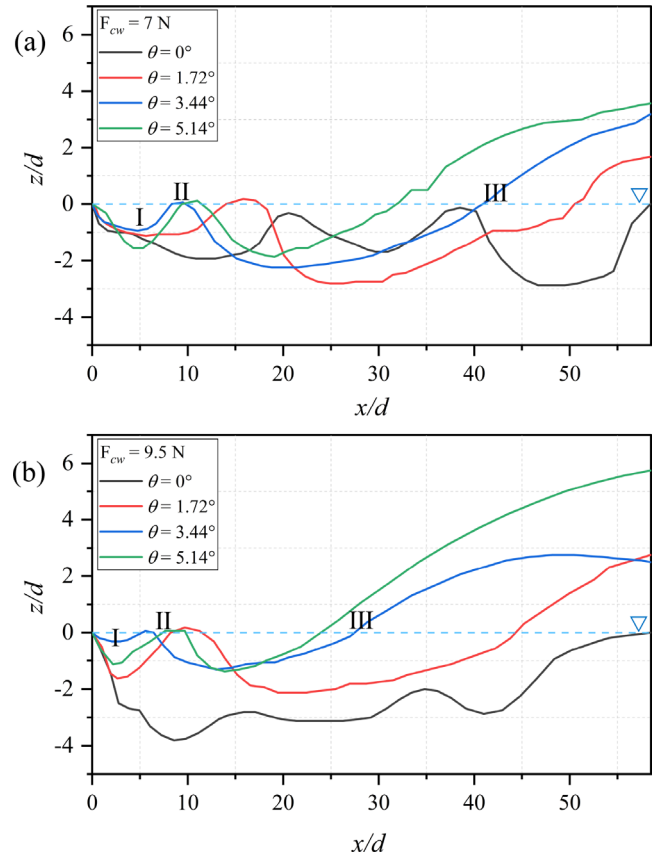

FIG. 3. The trajectories of the center of a buoyant sphere pulled by counterweights of (a) $F_{cw} = 7$ N and (b) $F_{cw} = 9.5$ N are presented for four different pulling angles in the x–z plane. The original air–water interface is marked by the blue dashed line. I—represents an air-cavity formation at the end of the first downward oscillation of the sphere away from the free surface; II—generation and pull-down of a horizontal air cavity; III—water exit of a sphere. Note the vertical axes have been expanded by a factor of three compared to the horizontal to make the data easier to read. Multimedia available online.

profiles in the x–z planes [Figs. 5(a) and 5(b)] for the same two cases, $F_{cw} = 7$ and $F_{cw} = 9.5$. These data show large increases in the overall velocities spanning the range $U = 0.9 - 8$ m/s. This is similar to the regime with a high Froude number ($Fr > 1.2$) that we observed in our previous investigation.[10] The remaining sphere trajectories for the other cases are provided in the supplementary Figs. S2–S4.

Deviation from a straight motion is commonly observed in free-falling sphere experiments investigated in the precrisis Reynolds number range.[12–14] The formation of swirling flows and vortices in the sphere's wake generates transverse forces pushing the sphere away from falling in a straight line. These vortices often have a helical component, further breaking the axial symmetry of the sphere's motion and affecting its path.[12–23] Horowitz and Williamson[12] mapped the different oscillations of free-falling and free-rising spheres depending on the Reynolds number and the ratio of the sphere to fluid density. They distinguish several regimes agreeing with the shedding of single- and double-sided vortex rings and a novel regime involving the
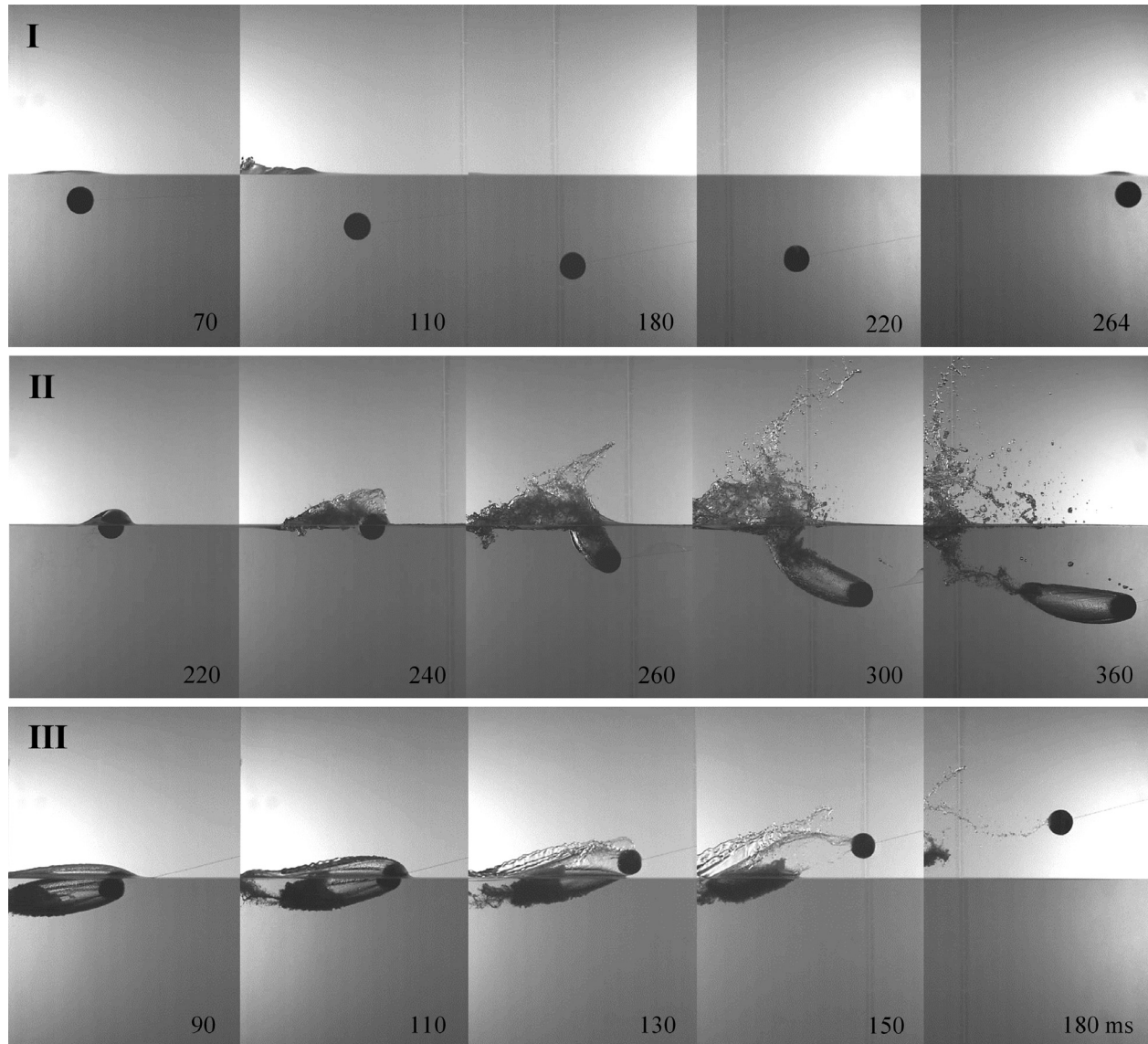
FIG. 4. I—An image sequence of the oscillatory sphere movement below and up to the water surface; II—a sequence of images illustrates the generation of a horizontal air cavity. The sphere is pulled at $\theta = 3.44°$ and a counterweight of $F_{cw} = 7$ N. $t = 220$ ms corresponds to the location where the sphere appears after the underwater oscillation $x/d = 7$, while $t = 240$ corresponds to $x/d = 10$, where the formation of the air cavity begins, $t = 260$ continuation of the formation of an air cavity in the wake of the sphere, $t = 300$ detachment of the aircavity from the interface and $t = 360$ corresponds to $x/d = 20$, marking the pinch of a stable air cavity. III—a sequence of images showing the water exit and rupture of the liquid layer above the air cavity of a sphere pulled at $\theta = 3.44°$, and a counterweight of $F_{cw} = 7$ N. $t = 90$ corresponds to $x/d = 37$, $t = 110$ moments of the sphere before water exit, while $t = 130$ to 180 corresponds to $x/d = 42$ to 50 marking the water exit of the sphere with the attached cavity and the formation of a rupture zone as the sphere leaves the surface. Multimedia available online.;

shedding of four vortex rings. In our experiments, we assume that the sphere oscillations and deviating from the straight path at $\theta = 0°$ are similar to those reported in the literature while also being influenced by the presence of the free surface, which additionally breaks the geometric symmetry.

Increasing the pulling angle promotes a faster rise of the sphere toward the fluid interface, thereby less opportunity for underwater oscillations to occur. Notably, the number of oscillations reduces with increasing θ, and the sphere's behavior changes: after the first dive, following the start of motion, the sphere rises toward the surface, piercing it without entering the air, rather it dives again generating an attached air cavity. This moment is identified in Figs. 3(a) and 3(b) as well as in Fig. 4(II) with Roman numerals for all cases where the pulling angles $\theta > 1°$ (i.e., near $\sim x/d = 10$). In these cases, the second cycle results in water exit as the sphere reaches the interface. All additional cases can be found in the supplementary material.
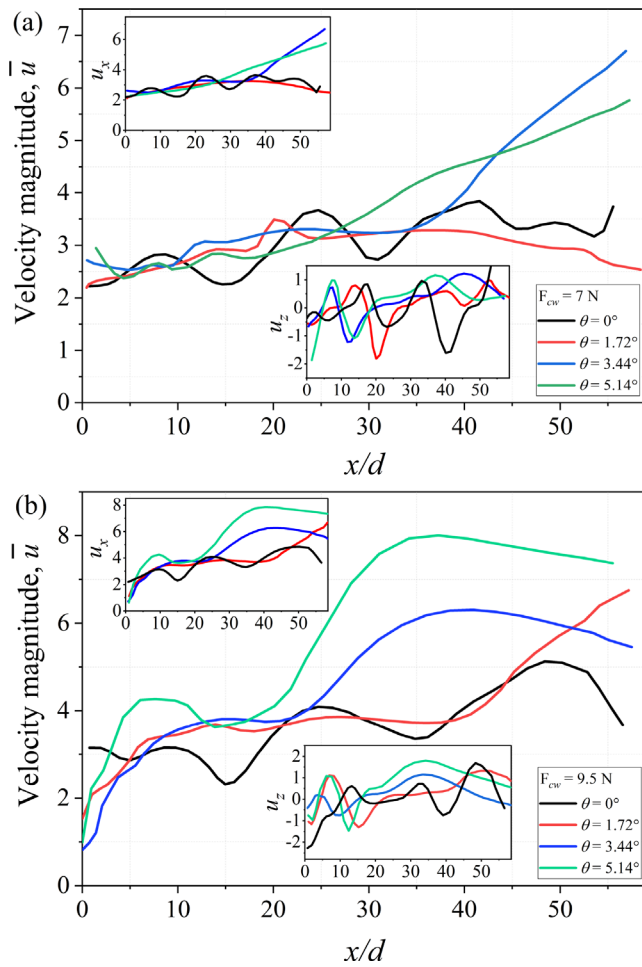
FIG. 5. The velocity magnitude for two selected pulling forces, (a) $F_{cw} = 7$ and (b) $F_{cw} = 9.5$ N at all pulling angles. The insets show the velocity components in the u_x and u_z. The colored lines depict the pulling angles as marked in the legend.

$t = 300$–360 ms. The closure of the splash curtain prevents further air from entering the cavity.[24] The surrounding fluid's hydrostatic pressure impedes the cavity's outer growth and initiates its detachment from the interface. Inertia then causes the cavity to pinch off into two parts at the closure stage, a lower cavity fully attached to the sphere and a chaotic upper splash cavity connected to the free surface. The subsurface air cavity continues to stretch and curve as the sphere moves through the water in a curved path corresponding to Fig. 3(a), e.g., between $x/d = 10$ and 42 for $\theta = 3.44°$. The air cavity attached to the sphere remains stable and moves horizontally for a short period, even though the pulling angle is $\theta > 1°$ toward the free surface. The air cavities are similar to those formed during free-falling sphere-impact experiments,[25–29] yet they are horizontal similar to spinning spheres[26] and half hydrophobic-/hydrophilic-coated spheres[30–32] and have somewhat helical patterns[33] on their surfaces. The length of the elongated cavity (l) varies, typically between $l/d = 5$ and 7, although it can reach up to 10 in some instances. Other studies report on cavity size at pinch-off however, the most relevant measurement to this study is likely those where the attached bubble becomes constant and persists far downstream. Vakerelski et al. showed that these cavities can also greatly reduce drag and reported values of $l/d = 3.71$–6.2.[29] Other water entry studies report on cavity sizes usually around pinch-off however, the cavities change size as they stabilize to balance pressure forces (e.g., Aristoff et al.[27] reported water entry bubbles attached to cavities of various $l/d \approx 2$ to 7.5 at pinch-off).

Figure 4(III) captures the moment when the sphere with the attached cavity reaches the free surface and exits into the air. The small bubble on the far left of ($t = 90$ ms) outside the main cavity rises to the surface indicated in $t = 110$ ms. The small bubbles near the water surface reveal a visible boundary between the collapsed cavity and the water surface, indicating the formation of a rupture zone ($t = 110$–150 ms) as the sphere leaves the surface and transits to the skipping mode ($t = 150$–180 ms). The evolution of main bubble collapse, small bubble motion, and splash formation near the surface highlights the complex interaction between the fluid, air, and solid. The angle of the exiting sphere is measured and compared in Fig. S8 [where, $\theta_s = \operatorname{atan}(y_{pulley}/x_{exit})$] revealing that θ_s is inversely proportional to F_{cw} and θ as one might expect.

It is important to note that during the experiments, the spheres traveled far from the horizontal plane of the water surface after the water exit. The vertical component of the pulling force obviously has some influence on the sphere's motion in the air, keeping the sphere out of the water. We did not focus extensively on the behavior after the water exit.

B. Sphere motion and force characteristics

The changing velocity of the sphere with time in Cartesian coordinates is shown in Fig. 5 for two different counterweights and four pulling angles. Figure 5 shows the velocity profiles of the spheres in the u_x and u_z directions, for three pulling angles $\theta > 1°$ cases and as well as for two pulling counterweights, $F_{cw} = 7$ N and $F_{cw} = 9.5$ N. At $\theta = 0°$, the sphere experiences a variation in the velocity magnitude oscillations below the water surface, with a range of 2–5 m/s for higher pulling counterweight cases. However, increasing the pulling angle $\theta > 1°$ results in faster sphere movement and acceleration through the bulk of water before exit. The sphere also returns to the surface more quickly.

Figure 4(II) contains a sequence of images depicting the evolution of the air cavity with the counterweight of $F_{cw} = 7$ N and pulling angle $\theta = 3.44°$. As mentioned earlier, this regime is achieved after one or two oscillations, and the sphere approaches the water interface with a waterline close to its center. Figure 4(II) shows that the free surface is deformed, and a splash exit is formed in the wake of the sphere passing through the free surface ($t = 220$–240 ms). As the sphere exits the water, a larger lift force is formed on the bottom of the sphere, resulting in the sphere diving ($t = 240$ ms). An air cavity is also formed by air entrained in the wake of the sphere. The air cavity continues to form in the wake of the sphere until $t = 300$ ms. The path of the sphere is curved as the sphere becomes fully submerged. The full submergence results in a more even lift force (i.e., horizontal motion), but the now deeper sphere experiences a larger upward tension force from the line attached to the pulley (i.e., $\theta(t)$ is increasing from $t = 260$ to 360 ms).

Figure 4(II) also illustrates the detachment of the subsurface air cavity from the interface, which quickly becomes nearly horizontal at

Higher pulling angles increase the velocity magnitude, reaching up to $\bar{u} = 8$ m/s after water exit. In some instances, the sphere experiences increased resistance and wake effects, causing it to lose vertical momentum upon reaching the air–water interface before generating the air-cavity formation. The sphere encounters a large downward lift force as it approaches the free surface for the first time at low velocities. These velocity changes are evident in the insets of u_z. However, the magnitude of u_z is still small compared to u_∞, resulting in an average $\bar{u}$ that changes less significantly. The generation of air-cavity moments is a feature of pulling angles $\theta > 1°$, which impacts the velocity magnitude for all cases. All additional velocity profiles for other non-selected cases are provided in the supplementary Figs. S2–S4.

The forces experienced by the sphere can be inferred from the position and velocity data obtained by image processing of video frames, similar to the method of Epps et al.[34] A free-body diagram of the sphere is sketched in Fig. 6. The hydrodynamic forces acting on the sphere can be split into several components, including the gravitational force F_g, the buoyancy F_B, the tension or counter-weight force F_{cw}, the drag force F_D, and the lift force F_L. The magnitude and direction of these forces depend on the pulling angles and velocity and shape and size of the air cavity.

The equation of motion can be written in the frame of reference of the sphere to find the drag and lift profiles as

$$F_D = -mg \sin\phi - (m + m_a)\dot{V}_s + F_B \sin\phi + F_{cw}\cos(\beta - \phi), \quad (1)$$

$$F_L = mg \cos\phi + (m + m_a)\dot{V}_n - F_B \cos\phi - F_{cw}\sin(\beta - \phi), \quad (2)$$

where m is the sphere's mass, $\dot{V}_s$ is the acceleration in the direction of the sphere motion, $\dot{V}_n$ is the acceleration orthogonal to the direction of the sphere motion, and $m_a = C_m\rho\forall$ is the sphere-added mass where we set $C_m = 0.5$ to reduce complexity and has been successfully implemented by other related studies.[35,36] Note the surface tension force is ignored as it is less than 1% of the gravitational force.

Figures 7(a) and 7(b) show how the drag and lift coefficients change with the distance moved by a sphere in the x direction normalized by its diameter, denoted by x/d for $F_{cw} = 7$ and $F_{cw} = 9.5$ N. The data start at the location where the sphere begins forming an air cavity until it exits the water at $\theta = 3.44°$. The drag coefficient fluctuates between $C_D = 1.1$ and $C_D = 0.3$ for $F_{cw} = 7$ N, while for $F_{cw} = 9.5$ N
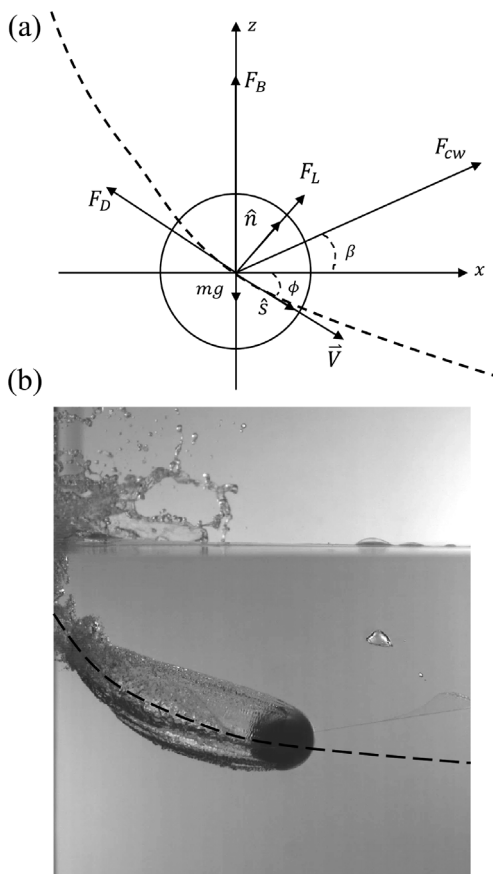

FIG. 6. (a) A free-body diagram showing the forces acting on the moving sphere. (b) Video frame showing the attached air cavity behind the sphere. The dashed line marks the curved trajectory of the sphere.
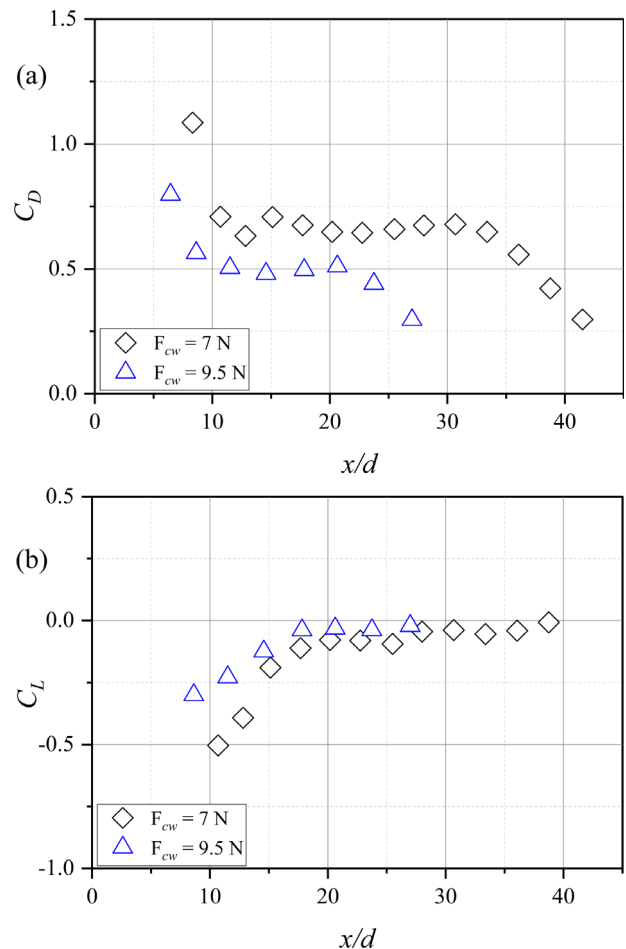

FIG. 7. The drag (a) and lift (b) coefficients are plotted as a function of x/d for two selected cases $F_{cw} = 7$ N (empty black diamonds) and $F_{cw} = 9.5$ N (empty blue triangles), from the moment the sphere begins forming an air cavity (e.g., $x/d = 6$–12) until it exits the water (e.g., $x/d = 25$–42) for $\theta = 3.44°$.

varied between $C_D = 0.8$ and $C_D = 0.3$ with corresponding Reynolds numbers in the range of $Re = 1.2 - 2.2 \times 10^5$. The drag coefficient is affected by the sphere generating waves and wakes at the air–water interface (e.g., $x/d = 6–9$), leading to an increase in drag force. On the other hand, the lift coefficient is affected by the formation of air cavities along the sphere's surface (e.g., $x/d = 8–12$), which changes the flow dynamics and increases lift. As the cavity stabilizes, the overall drag coefficient reduces to $C_D \approx 0.6$ for $F_{cw} = 7$ N and $C_D \approx 0.5$ for $F_{cw} = 9.5$ N, respectively. Because of the formation of an air cavity, the sphere's wetted surface area is smaller, which decreases the frictional forces and changes the pressure drag profile (aka form drag). The interaction of the lift and drag forces acting on the sphere generates uneven hydrodynamic pressures that force the sphere up and down in the water, as evident by the overall trajectories [Figs. 3(a) and 3(b)]. Hence, this effect becomes more pronounced as the sphere forms an air cavity and continues until it exits the water. Finally, increasing the pulling weight causes the sphere to exit the water sooner, which is also shown in Figs. 7(a) and 7(b). As expected, the current behavior differs from that observed for a traditional sphere moving in a bulk liquid, which experiences relatively uniform drag forces ($C_D \approx 0.5$) due to the surrounding fluid.[15]

C. Hydrodynamics of a sphere with a horizontal air cavity

This section discusses the novel hydrodynamic phenomenon observed in our experiments involving a sphere with an attached air cavity moving horizontally in the water. As demonstrated in Fig. 8 (Multimedia view), the sphere with an attached cavity at approximately the equator of the sphere ($\sim \pi/2$) has several moments in the trajectory where it maintains a steady horizontal motion at a constant velocity. The most obvious characteristics in Figure 8(a) are the inverted wing shape of the air cavity, which could generate negative lift forces to counter the combined sphere-cavity buoyancy and the

turbulent wake (visualized by the small bubbles trailing behind the cavity). This wing shape is also clearly visible in Fig. 4(II). In our experiments, the aspect ratio (L/D) of the air cavity length (L) to diameter (D) for all pulling counterweights ranged from 2 to 6 (see the supplementary material, Fig. S5). Because of the complexity of the problem here, we make a case study by considering one of the longest cavities [i.e., the cavity shown in Fig. 8(a)].

The horizontal sphere cavity can be compared with the recently discovered phenomenon of a stable-streamlined cavity formation following the impact of a free-falling sphere with a liquid interface.[28,29] Figure 8(b) shows an example of such a free-fall sphere cavity following the impact of a hydrophilic 15 mm steel sphere onto water.[29] The cavity assumes a self-determined streamlined shape, which, together with the free slip along the air cavity interface, results in a near-zero hydrodynamic drag. Considering only the steady horizontal motion of the sphere cavity allows us to simplify the force balance along the horizontal axis as $F_{cw} - F_D = 0$ and along the vertical axis as $F_B + F_L = 0$ shown in the free body diagram of Fig. 8(a).

Notice that we consider the total forces acting on the sphere cavity in this force balance. In this treatment, the sphere-cavity volume is the combined volume of the sphere with the attached cavity V_{SC}, and the effective density of the formation is given as m/V_{SC}. Using the standard expression for the drag on a sphere, $C_D = 2F_{cw}/\pi R^2 \rho U^2$, the drag coefficient of the formation is estimated to be $C_D \approx 0.5$, which is comparable to the drag on a sphere moving in the bulk fluid. If one accounts for the cross section at the widest part of the cavity instead of the sphere cross section in calculating the drag coefficient, C_D will be lowered by a factor of about ~ 2. Nevertheless, the drag on the horizontally pulled sphere cavity found here is much higher than the low drag on the free-falling sphere cavity found by Vakerelski et al.[29]

We assume that the turbulent wake observed behind the truncated cavity is a significant factor that contributes to the higher drag on the horizontally pulled sphere-cavity formation compared to the
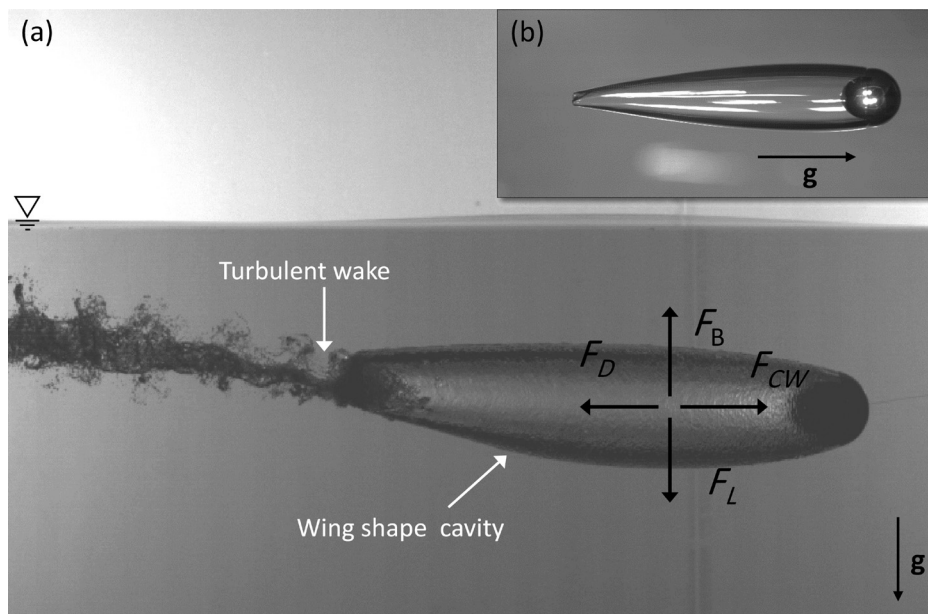

FIG. 8. (a) Snap-shot from the video showing the steady moving horizontal sphere with attached air-cavity formation using a pulling force $F_{cw} = 7$ N for $\theta = 1.72°$. Indicated is the force acting on the sphere-cavity formation, pulling force F_{cw} balanced by a drag force, F_D in a horizontal direction and buoyancy force, and F_B balanced by lift force F_L in a vertical direction. Inset (b) shows a free-falling sphere with an attached streamlined cavity formed following the impact of a 15 mm steel sphere on water reproduced with permission from Vakarelski et al., Soft Matter **15**, 6278–6287 (2019). Copyright 2019 Royal Society of Chemistry. Multimedia available online.

free-falling sphere cavity. The width of the wake visualized by the many small bubbles behind the cavity is comparable with the diameter of the sphere. The wake drag is the major contributor to sphere drag for this range of Reynolds numbers thus, it is not surprising that the overall drag is comparable to the drag on a submerged sphere without a cavity. In contrast, there is no noticeable wake behind the free-falling sphere cavity shown in Fig. 8(b), which leaves the flow behind the cavity relatively undisturbed.

The inverted wing shape of the horizontal cavity seen in Fig. 8(a) reveals the source of the significant downforce needed to keep the buoyant sphere cavity moving horizontally underwater. The buoyancy force is given by $F_B = g(\rho V_{SC} - m)$. Using an approximate value for V_{SC}, we obtain $F_B = -F_L \approx 6.5$ N, which is close to the magnitude of the pulling force used (F_{cw}). Finally, we can calculate the lift-to-drag ratio and find $F_L/F_D \approx 1$, which is not surprising for this moment in time where the sphere is at a constant horizontal velocity. One of the general findings of the free-falling sphere-cavity formation case was that the cavity size was self-adjusting in a way that kept the effective density of the sphere-cavity volume close to that of the displaced fluid (i.e., together, the sphere cavity was nearly neutrally buoyant). Similarly, in our case, F_{cw} can be considered an effective weight force that has a value close to F_B. We can then assume that, as in the case of free-falling sphere-cavity formation, the maximum volume of the cavity attached to the pulled sphere is determined by the same effective neutral buoyancy condition given by $V_{sc} < (F_{cw}/g + m)/\rho$. However, keep in mind that this is only an empirical observation so far.

One can assume the free-slip condition at the air-cavity interface for high Reynolds number regimes. This allowed for a potential flow treatment of the sphere cavity in the Vakerelski *et al.* study, which adequately described the physics of the steady falling sphere cavity.[28] Despite the substantial drag on the horizontally moving cavity, a potential flow model could sufficiently treat the lift force. In simplified terms, the bulged-down lower part of the cavity forces an acceleration of the flow below the cavity that, per the Bernoulli equation, will result in a downward lift force. However, the quantitative application of the potential flow model for the horizontally pulled cavity is complicated by its asymmetric shape, and we leave it for future investigation. Also, future research directions may investigate the effects of different sphere densities and the effect of superhydrophobic surfaces[37,38] on the hydrodynamics of buoyant objects.

IV. CONCLUSION

In this study, we investigated the dynamics of buoyant spheres accelerating horizontally at the air–water interface. We found that the behavior of the spheres becomes more irregular as the pulling force and speed increase. We see oscillatory motions with the sphere first diving down into the pool, followed by it rising toward and piercing the free surface before diving again, pulling attached underwater air cavities in the horizontal direction, thereby skipping under the surface. Unlike previous studies on skipping, our work investigated the effect of the pulling angle and strength of the pulling forces on the buoyant sphere hydrodynamics. Larger pulling angles resulted in different air-cavity lengths, larger skipping distances, and earlier water exit behavior. We found that drag and lift forces are similar for both pulling forces, but larger pulling forces achieve constant drag and lift more quickly.

Our findings also reveal that the sphere cavity maintains a steady horizontal motion at a constant velocity for a significant distance. The most characteristic features observed are the inverted wing shape of the air cavity and the turbulent wake behind the cavity. We analyzed the force balance on the moving sphere-with-cavity and estimated the drag coefficient to be $C_D \approx 0.5$. The buoyancy force of the formation was found to be close in magnitude to the pulling force used, and the lift-to-drag force ratio was approximately one. The higher drag on the horizontally pulled sphere cavity compared to the free-falling sphere cavity is likely due to the large, highly vortical wake observed behind the truncated cavity.

Our work provides a new understanding of the dynamics of buoyant spheres accelerated along an air–water interface and reveals rich physics that deserves further study. The findings have applications in various fields, such as marine engineering, underwater vehicles, and oceanography.

SUPPLEMENTARY MATERIAL

See the supplementary material for a photograph of the experimental laboratory setup (Fig. S1), additional non-selected trajectories and velocity profiles (Figs. S2–S4), and the description of the videos.

AUTHOR DECLARATIONS
Conflict of Interest

The authors have no conflicts to disclose.

Author Contributions

Farrukh Kamoliddinov: Data curation (lead); Formal analysis (supporting); Investigation (lead); Project administration (supporting); Supervision (equal); Validation (lead); Visualization (lead); Writing – original draft (lead); Writing – review & editing (equal). **Ivan Vakarelski:** Conceptualization (lead); Data curation (supporting); Formal analysis (supporting); Investigation (supporting); Methodology (supporting); Project administration (supporting); Supervision (supporting); Validation (lead); Visualization (lead); Writing – original draft (lead); Writing – review & editing (equal). **Sigurdur Tryggvi Thoroddsen:** Conceptualization (lead); Data curation (supporting); Formal analysis (supporting); Funding acquisition (lead); Investigation (supporting); Methodology (equal); Project administration (equal); Resources (lead); Supervision (equal); Writing – review & editing (equal). **Tadd T. Truscott:** Conceptualization (lead); Formal analysis (supporting); Funding acquisition (lead); Investigation (supporting); Methodology (equal); Project administration (supporting); Resources (lead); Supervision (equal); Validation (equal); Writing – review & editing (equal).

DATA AVAILABILITY

The data that support the findings of this study are available from the corresponding author upon reasonable request.

REFERENCES

[1] C. Clanet, F. Hersen, and L. Bocquet, "Secrets of successful stone-skipping," Nature **427**, 29–29 (2004).

[2] J. Belden, R. C. Hurd, M. A. Jandron, A. F. Bower, and T. T. Truscott, "Elastic spheres can walk on water," Nat. Commun. **7**, 10551 (2016).

[3] J. Glasheen and T. McMahon, "A hydrodynamic model of locomotion in the basilisk lizard," Nature **380**, 340–342 (1996).

[4] J. W. Bush and D. L. Hu, "Walking on water: Biolocomotion at the interface," Annu. Rev. Fluid Mech. **38**, 339–369 (2006).

[5] T. T. Truscott, B. P. Epps, and J. Belden, "Water entry of projectiles," Annu. Rev. Fluid Mech. **46**, 355–378 (2014).

[6] W. Johnson and S. Reid, "Ricochet of spheres off water," J. Mech. Eng. Sci. **17**, 71–81 (1975).

[7] L. Bocquet, "The physics of stone skipping," Am. J. Phys. **71**, 150–155 (2003).

[8] L. Rosellini, F. Hersen, C. Clanet, and L. Bocquet, "Skipping stones," J. Fluid Mech. **543**, 137–146 (2005).

[9] R. C. Hurd, J. Belden, A. F. Bower, S. Holekamp, M. A. Jandron, and T. T. Truscott, "Water walking as a new mode of free surface skipping," Sci. Rep. **9**, 6042 (2019).

[10] F. Kamoliddinov, I. U. Vakarelski, and S. T. Thoroddsen, "Hydrodynamic regimes and drag on horizontally pulled floating spheres," Phys. Fluids **33**, 093308 (2021).

[11] T. T. Truscott, B. P. Epps, and R. H. Munns, "Water exit dynamics of buoyant spheres," Phys. Rev. Fluids **1**, 074501 (2016).

[12] M. Horowitz and C. Williamson, "The effect of Reynolds number on the dynamics and wakes of freely rising and falling spheres," J. Fluid Mech. **651**, 251–294 (2010).

[13] P. Ern, F. Risso, D. Fabre, and J. Magnaudet, "Wake-induced oscillatory paths of bodies freely rising or falling in fluids," Annu. Rev. Fluid Mech. **44**, 97–121 (2012).

[14] I. U. Vakarelski, D. Y. Chan, and S. T. Thoroddsen, "Leidenfrost vapour layer moderation of the drag crisis and trajectories of superhydrophobic and hydrophilic spheres falling in water," Soft Matter **10**, 5662–5668 (2014).

[15] E. Achenbach, "Experiments on the flow past spheres at very high Reynolds numbers," J. Fluid Mech. **54**, 565–575 (1972).

[16] E. Achenbach, "Vortex shedding from spheres," J. Fluid Mech. **62**, 209–221 (1974).

[17] E. Achenbach and E. Heinecke, "On vortex shedding from smooth and rough cylinders in the range of Reynolds numbers 6×10^3 to 5×10^6," J. Fluid Mech. **109**, 239–251 (1981).

[18] P. W. Bearman, "Vortex shedding from oscillating bluff bodies," Annu. Rev. Fluid Mech. **16**, 195–222 (1984).

[19] H. Kim and P. Durbin, "Observations of the frequencies in a sphere wake and of drag increase by acoustic excitation," Phys. Fluids **31**, 3260–3265 (1988).

[20] H. Sakamoto and H. Haniu, "A study on vortex shedding from spheres in a uniform flow," J. Fluids Eng. **112**, 386–92 (1990).

[21] C. H. Williamson, "Vortex dynamics in the cylinder wake," Annu. Rev. Fluid Mech. **28**, 477–539 (1996).

[22] G. Yun, D. Kim, and H. Choi, "Vortical structures behind a sphere at subcritical Reynolds numbers," Phys. Fluids **18**, 015102 (2006).

[23] C. Kamble and S. Girimaji, "Characterization of coherent structures in turbulent wake of a sphere using partially averaged Navier–Stokes (PANS) simulations," Phys. Fluids **32**, 105110 (2020).

[24] M. M. Mansoor, J. Marston, I. U. Vakarelski, and S. T. Thoroddsen, "Water entry without surface seal: Extended cavity formation," J. Fluid Mech. **743**, 295–326 (2014).

[25] T. Grumstrup, J. B. Keller, and A. Belmonte, "Cavity ripples observed during the impact of solid objects into liquids," Phys. Rev. Lett. **99**, 114502 (2007).

[26] T. T. Truscott and A. H. Techet, "Water entry of spinning spheres," J. Fluid Mech. **625**, 135–165 (2009).

[27] J. M. Aristoff, T. T. Truscott, A. H. Techet, and J. W. Bush, "The water entry of decelerating spheres," Phys. Fluids **22**, 032102 (2010).

[28] I. U. Vakarelski, E. Klaseboer, A. Jetly, M. M. Mansoor, A. A. Aguirre-Pablo, D. Y. Chan, and S. T. Thoroddsen, "Self-determined shapes and velocities of giant near-zero drag gas cavities," Sci. Adv. **3**, e1701558 (2017).

[29] I. U. Vakarelski, A. Jetly, and S. T. Thoroddsen, "Stable-streamlined cavities following the impact of non-superhydrophobic spheres on water," Soft Matter **15**, 6278–6287 (2019).

[30] T. T. Truscott and A. H. Techet, "A spin on cavity formation during water entry of hydrophobic and hydrophilic spheres," Phys. Fluids **21**, 121703 (2009).

[31] D. A. Watson, J. M. Bom, M. P. Weinberg, C. J. Souchik, and A. K. Dickerson, "Water entry dynamics of spheres with heterogeneous wetting properties," Phys. Rev. Fluids **6**, 044003 (2021).

[32] A. Techet and T. Truscott, "Water entry of spinning hydrophobic and hydrophilic spheres," J. Fluids Struct. **27**, 716–726 (2011).

[33] M. M. Mansoor, I. U. Vakarelski, J. Marston, T. T. Truscott, and S. T. Thoroddsen, "Stable–streamlined and helical cavities following the impact of Leidenfrost spheres," J. Fluid Mech. **823**, 716–754 (2017).

[34] B. P. Epps, T. T. Truscott, and A. H. Techet, "Evaluating derivatives of experimental data using smoothing splines," in *Mathematical Methods in Engineering International Symposium* (IPC, Coimbra, Portugal, 2010), pp. 29–38.

[35] D. A. Watson, J. L. Stephen, and A. K. Dickerson, "Jet amplification and cavity formation induced by penetrable fabrics in hydrophilic sphere entry," Phys. Fluids **30**, 082109 (2018).

[36] D. A. Watson, C. J. Souchik, M. P. Weinberg, J. M. Bom, and A. K. Dickerson, "Making a splash with fabrics in hydrophilic sphere entry," J. Fluids Struct. **94**, 102907 (2020).

[37] A. Jetly, I. U. Vakarelski, and S. T. Thoroddsen, "Drag crisis moderation by thin air layers sustained on superhydrophobic spheres falling in water," Soft Matter **14**, 1608–1613 (2018).

[38] I. U. Vakarelski, F. Kamoliddinov, A. Jetly, and S. T. Thoroddsen, "When superhydrophobicity can be a drag: Ventilated cavitation and splashing effects in hydrofoil and speed-boat models tests," Colloids Surf., A **628**, 127344 (2021).